Title

A feasibility study on monitoring the evolution of apparent diffusion coefficient decrease during thermal ablation

Journal

Medical Physics, 42(9)

ISSN

0094-2405

Authors

Plata, Juan C
Holbrook, Andrew B
Marx, Michael
et al.

Publication Date

2015-09-01

DOI

10.1118/1.4928155

Peer reviewed

A feasibility study on monitoring the evolution of apparent diffusion coefficient decrease during thermal ablation

Juan C. Plata,[a] Andrew B. Holbrook, and Michael Marx
Department of Radiology, Stanford University, 1201 Welch Road, Stanford, California 94305

Vasant Salgaonkar and Peter Jones
Department of Radiation Oncology, University of California San Francisco, 1600 Divisadero Street, Suite H-1301, San Francisco, California 94143

Aurea Pascal-Tenorio and Donna Bouley
Department of Comparative Medicine, Stanford University, 300 Pasteur Drive, Edwards R321, Stanford, California 94305

Chris Diederich
Department of Radiation Oncology, University of California San Francisco, 1600 Divisadero Street, Suite H-1301, San Francisco, California 94143

Graham Sommer and Kim Butts Pauly
Department of Radiology, Stanford University, 1201 Welch Road, Stanford, California 94305

(Received 9 February 2015; revised 22 July 2015; accepted for publication 25 July 2015; published 10 August 2015)

Purpose: Evaluate whether a decrease in apparent diffusion coefficient (ADC), associated with loss of tissue viability (LOTV), can be observed during the course of thermal ablation of the prostate.
Methods: Thermal ablation was performed in a healthy *in vivo* canine prostate model ($N = 2$, ages: 5 yr healthy, mixed breed, weights: 13–14 kg) using a transurethral high-intensity ultrasound catheter and was monitored using a strategy that interleaves diffusion weighted images and gradient-echo images. The two sequences were used to measure ADC and changes in temperature during the treatment. Changes in temperature were used to compute expected changes in ADC. The difference between expected and measured ADC, ADC_{DIFF}, was analyzed in regions ranging from moderate hyperthermia to heat fixation. A receiver operator characteristic (ROC) curve analysis was used to select a threshold of detection of LOTV. Time of threshold activation, t_{LOTV}, was compared with time to reach $CEM_{43} = 240$, t_{DOSE}.
Results: The observed relationship between temperature and ADC *in vivo* (2.2%/°C, 1.94%–2.47%/°C 95% confidence interval) was not significantly different than the previously reported value of 2.4%/°C in phantom. ADC_{DIFF} changes after correction for temperature showed a mean decrease of 25% in ADC 60 min post-treatment in regions where sufficient thermal dose ($CEM_{43} > 240$) was achieved. Following our ROC analysis, a threshold of 2.25% decrease in ADC_{DIFF} for three consecutive time points was chosen as an indicator of LOTV. The ADC_{DIFF} was found to decrease quickly (1–2 min) after reaching $CEM_{43} = 240$ in regions associated with heat fixation and more slowly (10–20 min) in regions that received slower heating.
Conclusions: Simultaneous monitoring of ADC and temperature during treatment might allow for a more complete tissue viability assessment of ablative thermal treatments in the prostate. ADC_{DIFF} decreases during the course of treatment may be interpreted as loss of tissue viability.
 [http://dx.doi.org/10.1118/1.4928155]

Key words: tissue viability monitoring, apparent diffusion coefficient, MR thermometry, thermal therapies

1. INTRODUCTION

Prostate cancer continues to be the most common type of cancer found in American males. In addition, benign prostate hyperplasia (BPH) affects more than 50% of men over the age of 60[1] and leads to urinary incontinence and a decreased quality of life. Minimally invasive therapies based on heating-induced coagulative necrosis[2–5] have been developed to help treat patients with these conditions. For prostate cancer, the heating is intended to destroy the tumor, whereas in BPH, healthy tissue is destroyed in order to relieve pressure on the urethra. MRI has emerged as a promising modality to monitor these treatments due to its ability to noninvasively measure temperature changes during treatment, as well as its flexible contrast modalities for treatment planning and evaluation.[6]

Thermal dose monitoring is used to determine whether a tissue has been exposed to enough thermal energy to undergo coagulative necrosis.[7–9] For the prostate, a thermal dose of

cumulative equivalent minutes at 43 °C (CEM_{43}) greater than 240 is commonly used as the threshold to indicate loss of tissue viability (LOTV).[10] The relationship to compute CEM_{43} is[11]

$$\mathrm{CEM}_{43} = \int_0^t R^{T(\tau)-43} d\tau,$$

where $R = 2$ for $T(\tau) > 43$ °C and $R = 4$ for $T(\tau) < 43$ °C. It is worth noting some of the limitations of this metric. First, thermal dose is based on absolute temperature, which is not readily available using conventional proton resonant frequency based MR thermometry, which can only measure temperature changes.[6] In order to estimate absolute temperature, one must assume a baseline temperature, typically 37 °C, or measure temperature discretely using temperature probes, which may not be available for noninvasive and minimally invasive applications. Additionally, thermal dose relies on models to estimate tissue viability but cannot directly measure tissue changes. For this reason, other metrics such as diffusion and perfusion changes are often used to verify the amount of tissue that has been treated.[12]

Diffusion weighted MRI (DWI) has been used to compute apparent diffusion coefficient (ADC) maps that can help plan, monitor, and assess these treatments.[12,13] Previous studies have demonstrated a 36% reduction in the ADC following either cryoablation or high intensity ultrasound induced tissue damage of the prostate.[13] As a result, unlike thermal dose, the origin of the signal used to compute ADC is irreversibly changed by loss of viability. This makes ADC a promising metric for monitoring viability changes. The origin of this decrease is still unknown. However, because this result was seen for both thermal and cryoablation lesions in the prostate, as well as in the treatment of other tissues such as uterine fibroids,[14,15] the decrease in ADC could be generalizable to loss of viability. Potential reasons for a decrease in ADC include decreased molecular activity due to protein denaturation, reduced cellular motility from loss of viability, and/or reduced perfusion from compromised vasculature. In comparison to contrast-enhanced MRI (CE-MRI), the current gold standard for measuring loss of tissue viability, measuring changes in ADC does not depend on any exogenous contrast and therefore can be used repeatedly. CE-MRI can only be used to assess treatment once, since regions that are already perfused with contrast will continue to receive signal enhancement due to contrast retention across subsequent treatments, regardless of whether or not the tissue was successfully treated in those treatments. An endogenous contrast, such as ADC, that indicates tissue viability and could be measured repeatedly would allow for improved treatment guidance and monitoring.

Prior work has simultaneously acquired ADC and temperature[16] in order to use the ADC information to correct for temperature drift in a gel phantom. In that case, all ADC changes were due to temperature, uncomplicated by ADC changes in tissue from ablation. In this work, we want to do the opposite: draw out ADC changes in tissue from ablation by correcting for temperature-induced ADC changes.

Therefore, in this work, ADC and temperature were monitored concurrently during thermal ablation of the prostate in order to remove temperature effects from the ADC measurement and study the evolution of the ADC decrease previously reported. The purpose of this work was then to assess whether monitoring the evolution of the ADC decrease could provide insight into treatment outcome.

2. METHODS

2.A. Transurethral ultrasound applicator

The catheter-based transurethral ultrasound applicator (Fig. 1) consists of two multisectored tubular transducers mounted on the distal portion of a flexible Pebax multilumen delivery catheter. Each tubular transducer segment [3.5 mm outer diameter (OD), 10 mm long, $f \cong 7$ MHz] has two separate 120° active sectors with independent power control and a 120° inactive sector. This design allows for 3D control of the angle and length of energy deposition and heat delivery. The transducer assembly is enclosed in an expandable PET urethral cooling balloon (10 mm OD),[17] inflated after insertion with temperature regulated water flow for coupling and to cool the urethral mucosa. A separate distal bladder balloon is inflated to position and anchor the device, in order to prevent motion during the treatment.

2.B. Animal model and ultrasound ablation

All animal experiments were reviewed and approved by our institution's Administrative Panel on Laboratory Animal Care (APLAC). Two adult mixed breed dogs with healthy prostates were treated under general anesthesia (1% to 4% isoflurane gas anesthesia). The MR-compatible catheter-based ultrasound applicator was inserted into the urethra and anchored using an expandable bladder balloon. Right and left anterior sides of the prostate were heated for study 1, and the right posterior side of the prostate was treated for study 2. For each sonication, the temporal average intensity at the transducer surface was 7.6–9.5 acoustic W/cm^2 for 9 min. The treatments created lesions of approximately 1 cm radial distance from the cooled urethral wall. In order to record the baseline temperature prior to treatment, a Luxtron probe was placed on the endorectal (ER) coil. Active cooling did not start until MR monitoring had started and approximately 1 min of baseline images had been acquired. For study 1, applied power and duration were controlled to preserve the boundary of the

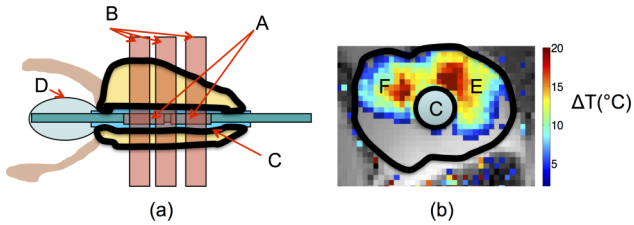

FIG. 1. (a) Ultrasound applicator schematic (b) MR temperature image (right, axial view). The prostate is outlined in black. A. Multisectored tubular transducers (3×10 mm long, dual 120°), B. monitoring slices, C. 10 mm cooling balloon, D. bladder anchoring balloon, E. sector #1 heating pattern, F. sector #2 heating.

prostate for histological tracing between treated and untreated tissues. Following a cooling period of approximately 25 min, the left anterior side of the prostate was heated a second time. For study 2, treatment was restricted to a small region of untreated tissue and only 3 min of cooling data were collected due to scheduling restrictions. The animals were euthanized and the prostate was harvested for histological analysis within 2 h following treatment.

2.C. MRI monitoring

A 3T GE MR750 scanner was used for MR imaging. The scanner's body coil was used to transmit RF and two receiver coils (5 in. surface coil and ER coil) were used for signal acquisition. RTHawk (HeartVista, Inc., Menlo Park, CA) was used to prescribe the MR sequences, reconstruct acquired images, and display the images through a custom interface.[1,17,18] MR thermometry and diffusion weighted sequences (Table I) were continuously interleaved during treatment, and the first acquired frame after each sequence change was discarded to ensure that all recorded measurements were at steady state. Three axial slices were monitored for study 1, and a single axial slice was monitored for study 2. Images were updated every 17 s. ADC maps were calculated as the arithmetic mean of the ADCs obtained from three orthogonal directions. For each direction, ADC was computed as[19]

$$\mathrm{ADC} = -\frac{\log\left(\frac{M_{b2}}{M_{b1}}\right)}{(b_2 - b_1)},$$

where $b_2 = 1000$ s/mm^2 and $b_1 = 0$ s/mm^2 and M_{b2} and M_{b1} are the corresponding magnitude diffusion weighted images. Following treatment, 3D contrast enhanced $T1$ weighted scans were acquired to assess tissue viability.

2.D. Prostate histology

The resected prostates were fixed in 10% buffered neutral formalin for approximately one week and then sliced into sections approximately 5 mm thick along the axial plane to approximate the MR monitoring scan planes. Fixed sections were then prepared for paraffin embedding, and 4 μm thick histology slices were cut and stained with hematoxylin and eosin (H&E). Slides representing slices of interest were digitized and traced using SEDEEN VIEWER (PathCore, Toronto, ON CA) software to outline and measure lesion size. Due to prior thermal lesions surrounding the region treated for study 2, tracing was not possible for this specimen.

TABLE I. Imaging parameters.

	Thermometry	ADC[a]	CE-MRI[b]
Type of sequence	SPGR[c]	SE[d]	GE[e]
Readout	Cartesian	ssEPI[f]	Cartesian
TE/TR (ms)	8/35	80eff/1125	2.64/5.27
FOV (cm)	15	15	12
Resolution (mm)	1.17	2.34	0.469
Flip angle (deg)	10	90	30
Slice thickness (mm)	5	5	2
Bandwidth/pixel (Hz)	244	1953 (readout), 16 (phase encode, effective)	976

[a]Apparent diffusion coefficient (ADC).
[b]Contrast enhanced (CE).
[c]Spoiled gradient echo (SPGR).
[d]Spin echo (SE).
[e]Gradient echo (GE).
[f]Single-shot echo-planar imaging (ssEPI).

2.E. Image registration

Unless otherwise stated, all analysis was performed using MATLAB (The Mathworks, Inc., Natick, MA). In order to register the changes in temperature with their respective changes in ADC, all ADC maps were upsampled to a 128×128 grid using a cubic interpolation. Masks generated by manually segmenting the prostate from the gradient-echo (GRE) and single-shot echo-planar imaging (ssEPI) acquisitions were used to align the two datasets, using two-dimensional cross-correlation. Segmentation was performed by a graduate student with 3 yr experience on identifying prostate anatomy. Phase maps prior to tissue heating were used to estimate $B0$-induced off-resonance maps (Fig. 2). Estimated off-resonance maps were unwrapped using Goldstein's branch cut method[20] and then used to warp the temperature change maps in order to match the off-resonance warping in the ssEPI images. Specifically, off-resonances were converted to expected shifts in the phase encoding direction based on the ssEPI bandwidth in the phase-encoding direction. Pixel values were then shifted[21] and resampled into a uniform grid using a Gaussian kernel interpolation. Through this process, coregistered temperature and diffusion images were generated with similar low bandwidth shift artifacts. No shifts were performed in the frequency encoding direction because the per-pixel bandwidth was high enough for both sequences to tolerate temperature dependent geometrical distortions. Image registration was assessed by verifying that the location of the hotspots in both images was on average no more than 2 pixels apart. If the hotspot locations did not match, the unwrapped phase image was examined for discrepancies and the registration process was iterated. To prevent noisy data from shifting into the region of the prostate, the prostate was manually segmented and noise

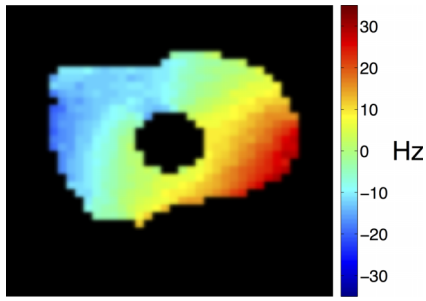

FIG. 2. $B0$ unwrapped off-resonance map in Hz. Phase images prior to heating were used as $B0$ maps to determine expected pixel shifts from the low bandwidth ssEPI. Unwrapping was performed using Goldstein's branch cut method. The mask obtained from manual outlining of the prostate was used to highlight the area of interest.

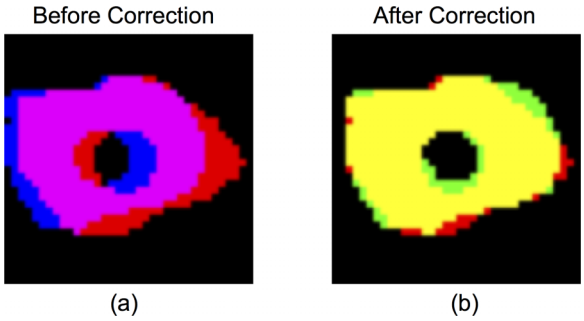

FIG. 3. Mask overlay comparison (a) before and (b) after correction. The prostate was manually outlined to generate masks from the diffusion weighted ssEPI image (red), GRE image (blue), and overlap (purple) before correction. The mask from the GRE image was warped using the B0 map shown in Fig. 2 and aligned using a 2D cross correlation to generate the corrected mask (green), ssEPI image (red), and the overlap (yellow).

regions were masked out prior to application of the cross-correlation alignment. The resulting masks and their alignment are compared in Fig. 3. Finally, since ADC and temperature measurements were interleaved, a linear interpolation in time was used to approximate the ADC values at the times when the temperature measurements were collected. Both ADC and temperature time histories were smoothed using a five point moving average filter for improved SNR.

2.F. Linear model for computing estimated ADC

Measurements were made in 3×3 voxel regions of interest (ROIs) in both the ADC and temperature images. The high signal originating from the cooling balloon in the $T2$-weighted ssEPI images was used to generate a mask and remove ROIs near the cooling balloon, to avoid partial volume effects from the circulating water. To determine the relationship between ADC and temperature in the absence of tissue destruction, all data with a change in temperature less than 8 °C were used to find the 1st order fit between changes in temperature and their associated changes in ADC. A threshold of 8 °C was chosen since no thermal damage would be expected for 240 min under these conditions using our baseline temperature of 35 °C. Data that had seen changes in temperature greater than 8 °C were not included since tissue viability for these instances might have been compromised. The slope of this fit between %ADC increase and temperature increase will be referred to as β, with units of %ADC/ °C. To find this fit, the data were divided into 100 bins along the temperature increment axis, with the mean %ADC change found for each bin. To see how susceptible the fit was to noise in the data, the data in each bin were randomly resampled (bootstrapped) 1000 times. For each iteration, a least squares fit was used to estimate β. The mean β along with the 95% confidence interval was computed from these iterations.

2.G. Monitoring ADC decrease

Temperature measurements were converted into estimated ADC values using β. Prior to heating, the standard deviation

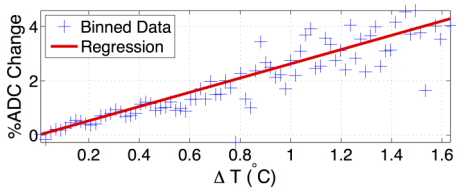

FIG. 4. Linear fit used to determine relationship between changes in temperature and changes in ADC. ADC changes and temperature changes for pixels that had not reached $CEM_{43} > 240$ were used as a training set to determine the relationship between %ADC change and change in temperature. Data for this fit were binned and averaged using 100 bins in the temperature axis.

(σ) of the measured ADC was computed across 10 time points for all ROIs and later used to determine a statistically significant threshold. The difference between the temperature-estimated ADC value and the measured ADC value, ADC_{Diff}, was calculated. Previous studies have correlated a decrease in ADC with LOTV.[12,13] For this study, LOTV was estimated to occur when ADC_{DIFF} decreased to below -2.25σ for three consecutive time points. This threshold was determined retrospectively using a receiver operating curve analysis detailed in Sec. 2.H. A decrease of that magnitude for that number of consecutive intervals will randomly occur with a probability of $(0.0122)^3 \approx 1.82 \times 10^{-6}$, assuming purely Gaussian noise. Representative ROIs were chosen for analysis in regions that received sublethal treatment ($CEM_{43} << 240$), marginal treatment ($CEM_{43} \approx 240$), and highly lethal treatment ($CEM_{43} >> 240$).

2.H. Viability map assessment

In order to assess the specificity and sensitivity of the proposed viability monitoring method, a logical map corresponding to voxels that had reached $CEM_{43} > 240$ was created and compared to logical maps of voxels that met the significant decrease criteria, LOTV, for different threshold settings. The final logical masks for $CEM_{43} > 240$ and LOTV were analyzed using a receiver operating characteristic (ROC) curve. The area under the curve (AUC) of the ROC was used to test the classifier and the point closest to [0 1] in the operating curve was used as the threshold for all further analysis,

$$\text{Sensitivity} = \text{True Positive} = \frac{(\text{LOTV}) \cap (\text{CEM}_{43} > 240)}{(\text{CEM}_{43} > 240)},$$

$$\text{Specificity} = \text{True Negative} = \frac{(!\text{LOTV}) \cap (\text{CEM}_{43} < 240)}{(\text{CEM}_{43} < 240)},$$

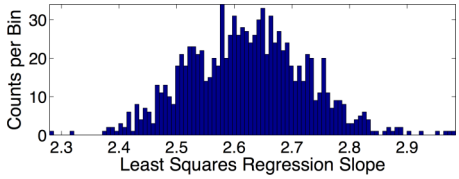

FIG. 5. Least square slope distribution bootstrapping analysis. Each bin was subsampled 1000 times. For each iteration, a least squares regression was performed to find a slope. A mean slope of 2.2%ADC/ °C with a 95% confidence interval of 1.94%–2.47%ADC/ °C was measured.

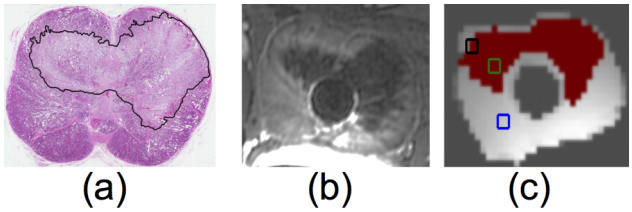

FIG. 6. Tissue viability validation. (a) H&E histology slice with damage zone outlined, (b) contrast-enhanced MRI post-treatment, and (c) artificially distorted GRE image with area that reached $CEM_{43} > 240$ shaded and monitoring ROIs overlaid. Three ROIs are $CEM_{43} = 10^6$ (green), $CEM_{43} = 494$ (black), and $CEM_{43} = 0$ (blue).

LOTV = Regions that have met the proposed criteria for loss of viability,

!LOTV = Regions that have not met the proposed criteria for loss of viability.

Using the true positive regions for the optimal classifier, and limiting the analysis to the region that only received one heat in order to remove ambiguity between the effects of the two treatments, the relationship between the amount of thermal dose delivered and the delay between triggering LOTV, t_{LOTV}, and reaching $CEM_{43} > 240$, t_{DOSE}, were characterized. This delay is referred to as t_{DELAY}.

3. RESULTS

3.A. ADC temperature linear model

The bootstrap analysis to estimate the relationship between changes in %ADC and temperature found average β of study 1 to be 2.2%ADC/°C (95% confidence interval of 1.94%–2.47%ADC/°C) and study 2 had an average β of 2.19% (95% confidence interval of 1.35%–3.02%ADC/°C). These values are not statistically significant from the 2.4%ADC/°C previously reported in phantom.[22] Figure 4 shows the linear fit for study 1, superimposed on the binned data. Figure 5 shows the distribution of slopes obtained for study 1. Due to lack of sufficient cooling data for study 2, only data from study 1 were used for the remaining analysis. Since β values for studies 1 and 2 were similar, yet more data were collected for study 1 (three slices compared to one), a β of 2.2%ADC/°C was chosen.

3.B. ADC decrease monitoring

Three example ROIs were chosen from regions of interest that reached sublethal ($CEM_{43} = 0$), marginal ($CEM_{43} = 494$), and highly lethal ($CEM_{43} = 10^6$) thermal dose. Tissue viability for these regions was verified using CE-imaging and H&E staining (Fig. 6). The ADC and temperature time histories for the sublethal ROI are shown in Fig. 7(a). ADC_{DIFF} never falls significantly below 2.25σ for more than three consecutive time points, and hence, LOTV is never reached. Time histories for the marginal thermal dose ROI are shown in Fig. 7(b). This example illustrates the proposed metric; an ADC_{DIFF} drop below the 2.25σ threshold for more than three time points was assumed to reflect LOTV. The t_{LOTV} for this ROI occurs at approximately 30 min, while t_{DOSE} occurs around 15 min. In this case, the ADC decrease appears to develop slowly after t_{DOSE} is reached. In comparison, the region that received a high thermal dose [shown in Fig. 7(c)] has a $t_{LOTV} = 12$ min and $t_{DOSE} = 10$ min, indicating a much sharper decrease in ADC and triggering of the LOTV monitoring.

3.C. Viability map assessment

The ROC curve comparing the LOTV classifier with thermal dose is shown in Fig. 8. The classifier has an AUC of 0.89. The optimal classifier obtained using the ROC curve was found to be a threshold of -2.25σ for three consecutive time points. This corresponds to a specificity 0.90 and a sensitivity of 0.87. The relationship between thermal dose delivered and

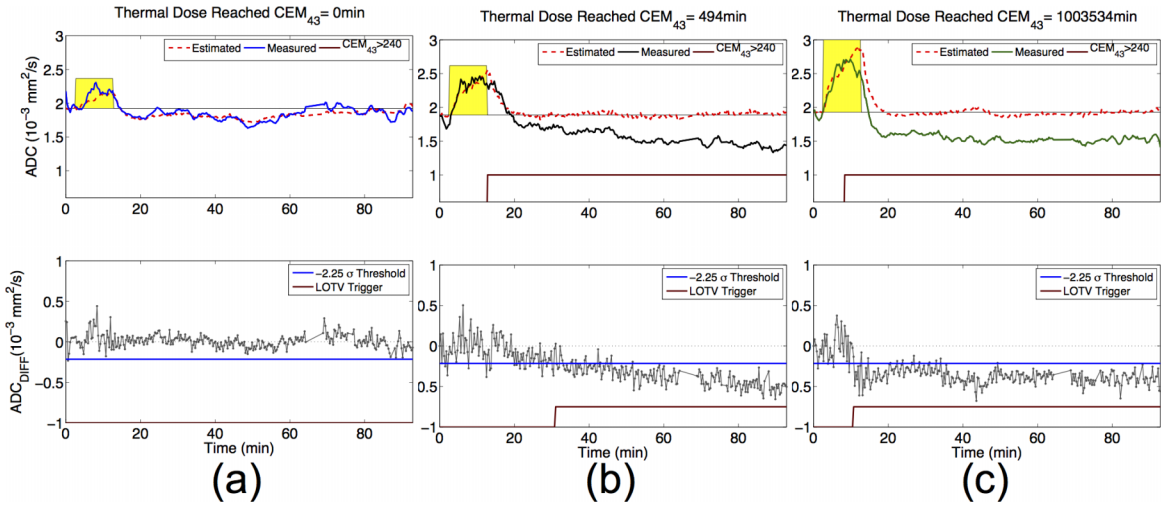

FIG. 7. Example time history for three regions of interest: sublethal (a), marginal (b), and highly lethal (c). Estimated (dashed) and measured ADC (solid) values are presented on the top plot along with a shaded region to indicate when ultrasound was on and a step function to indicate when $CEM_{43} > 240$ is reached. The bottom plot shows the evolution of ADC_{Diff} and a step function to indicate when LOTV is reached (when three consecutive time points have $ADC_{Diff} < 2.25\sigma$). The sublethal region does not see any significant changes in ADC_{Diff} while the marginal sees a slow change in ADC_{Diff} and the highly lethal treatment sees a more abrupt change in ADC_{Diff} close to the time when $CEM_{43} > 240$ is reached.

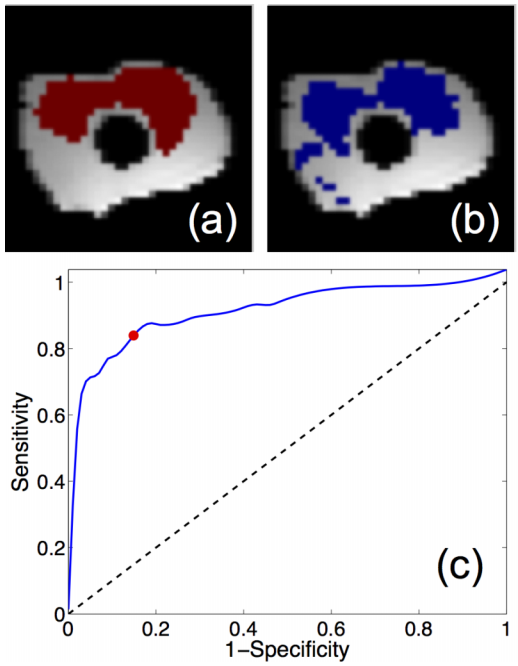

FIG. 8. Logical maps for regions that saw a $CEM_{43} > 240$ (a) in brown and logical map for regions where LOTV was triggered (b) in blue for the selected trigger settings of 2.25σ for three consecutive points. (c) shows a ROC curve with the optimal classifier settings highlighted by a red point. The ROC curve has an AUC of 0.89.

the delay between t_{LOTV} and t_{DOSE} are shown (Fig. 9). As previously noted, regions that saw high thermal doses had a shorter t_{DELAY} (seconds to a few minutes) compared to regions that saw marginal doses (tens of minutes).

4. DISCUSSION

The results of this study demonstrates that irreversible changes in ADC can be monitored during treatment. A linear model between %ADC/°C can be used to predict ADC changes based on temperature changes *in vivo*. Deviations from this model, ADC_{DIFF}, can be used to monitor for the ADC decrease that has been previously associated with loss of tissue viability post-treatment. Results show that the decrease in ADC develops at different rates depending on the amount of thermal dose, and how aggressively it was delivered to the tissue. This change in ADC might be used in future ablation treatments as both an indication that sufficient thermal dose has been delivered to destroy tissue and as a measure of the type of ablation that has occurred.

4.A. Linear model

A moderate linear relationship between %ADC and ΔT (average $R^2 = 0.8$ after binning) was found. The average slope was found to be 2.2%ADC/°C (95% confidence interval of 1.94%–2.47%ADC/°C) for study 1 and 2.19% (95% confidence interval of 1.35%–3.02%ADC/°C) for study 2. Both of these values were not found to be statistically different from the previously reported 2.4% ADC/°C. To the best knowledge of the authors, this is the first time that this relationship has been measured in an *in vivo* animal model. Although only two canine prostates are reported, four slices consisting of a total of 768 ROIs were analyzed. No statistically significant subject-to-subject variation of β was found in our two subjects. In this work, the β estimate was determined using only changes between consecutive time points, in order to make the computation more robust against slowly changing factors, such as perfusion and motion. For this reason, the temperature changes used in the β fitting were not very high. However, previous studies, which used molecular diffusion to monitor hyperthermia treatments in phantom, have acquired data that validate a similar linear relationship between %ADC and ΔT up to 46 °C.[22,23]

4.B. Evolution of ADC_{DIFF}

Monitoring changes in ADC_{DIFF} allowed for detection of irreversible ADC decreases during treatment. This is an improvement over simply using post-treatment ADC as an indicator for loss of tissue viability, since the progression of LOTV is available. How quickly ADC_{DIFF} decreased depended on how much dose was delivered and may provide insight into the type of cell death. Type of cell death could be important in knowing whether the tissue has potential for regeneration. Regions that saw highest thermal doses in this experiment experienced very quick heating associated with heat fixation (rapid denaturation of proteins), while regions that received lower doses likely did not experience heat fixation and could therefore have a higher regeneration potential.[24]

A period of ADC_{DIFF} increase was often present prior to an ADC_{DIFF} decrease that triggered LOTV [e.g., 0–20 min in Fig. 7(b) and 0–10 min in Fig. 7(c)]. Previous studies have reported that enhanced perfusion occurs as a result of heating,[25] which

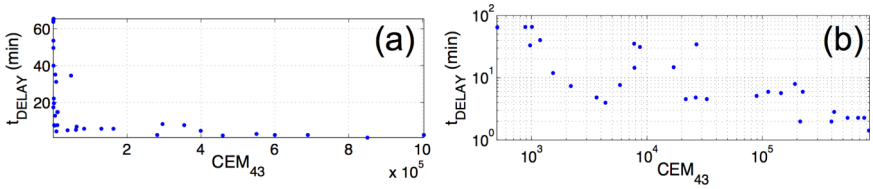

FIG. 9. Relationship between the delay for LOTV to be reached after $CEM_{43} > 240$ is reached, t_{DELAY}, and CEM_{240}. True positive regions on the side of the prostate that was only treated once were used to study this delay. Regions that receive sufficiently high thermal dose ($CEM_{43} > 10^5$) appear to have similarly low delay times compared to regions that receive marginal thermal doses (a). Plotting the relationship in a log–log scale highlights the continuously decreasing delay time with increasing dose (b).

may be responsible for this observation. This early increase in ADC_{DIFF} is no longer present after ablation presumably due to loss of blood flow.

4.C. Thermal dose as a metric for comparison

For this study, $CEM_{43} > 240$ was used as a ground truth to compare the LOTV logical maps. Since baseline temperatures were only available at the location where the Luxtron probe was placed, it is possible that the baseline temperature is not accurate for the whole gland. This could be a concern since baseline temperatures are required to compute thermal dose. A major advantage of the proposed strategy for assessing tissue viability is that it only relies on accurate measurements of temperature changes and is not dependent on accurate baseline temperature estimates. Thermal dose measurements are still available and can provide an immediate prediction of tissue response, which will be monitored using the LOTV. It is important to stress that although thermal dose and rate of thermal dose delivery can be obtained using PRF thermometry alone, the tissue response to the treatment is not being measured but rather only predicted. In contrast, the proposed method provides a metric that previous work has shown to be irreversibly affected by the loss of tissue viability.[13] More specifically, instead of inferring that a change happened to the tissue using a metric that is not sensitive to this change, such as temperature, a change in the tissue has been detected through ADC and attributed to lesion formation. Some possible sources for the decrease in ADC_{DIFF} include protein denaturation compromising regular molecular transport function and decreased perfusion currently used by CE-MRI to assess treatment volume.

4.D. Future work: Modifications for prospective studies

For the techniques presented in this work to be feasible for prospective guidance of treatment, a quicker and more accurate registration and improved signal to noise (for increased temporal resolution) are necessary. Specifically, higher pixel bandwidth of the ADC monitoring is necessary to reduce shift artifacts, and higher SNR of the ADC measurements is necessary to facilitate single voxel measurements without averaging. Along with higher pixel bandwidth, an accurate off-resonance map would allow for improved correction of remaining distortion artifacts. Improved registration between the ADC, temperature images, and histology will allow for more quantitative analysis. Higher SNR may be attained through optimization of b-value selection and of the pulse sequences.

The sensitivity of the viability monitoring can also be optimized for specific applications. For this analysis, a criterion of $ADC_{DIFF} < -2.25\sigma$ for three consecutive points was selected retrospectively to obtain reasonable true positive and true negative ratios without sacrificing the ability to detect sharp drops quickly. However, these parameters can be modified so that the detection of tissue changes is either more robust or more aggressive depending on the type of heating being delivered. Additional data, particularly with improved SNR, will help in determining appropriate thresholds for real time classification.

Although we present preliminary subject-to-subject variation, future studies will help strengthen this relationship. If β varies significantly between subjects, a low power calibration heating can be used to estimate it before ablative treatment. If β does not vary across subjects, a well-validated coefficient could be used for all treatments. Since this work was restricted to the treatment of healthy prostate tissue, treatments in different tissues, both healthy and cancerous, could help determine how generalizable this metric can be. Previous work in the fibroids[14,15] shows promise that ADC can also be a marker for thermal lesion formation in other organs.

5. CONCLUSIONS

In conclusion, initial results were presented that demonstrated the ability to assess tissue viability during treatment, using intrinsic tissue property changes. The proposed method successfully accounted for temperature induced ADC changes to observe ADC changes due to tissue response during thermal treatments. Appropriate thresholds allowed estimation of the timing of loss of tissue viability, which occurred quickly after aggressive ablation and took longer to develop in moderate ablation regions. It is possible that active monitoring of ADC may yield a more informative direct measurement of tissue viability than is achieved through thermal dose alone and improve treatment monitoring and prediction of treatment outcomes.

ACKNOWLEDGMENTS

This work was funded using NIH Grant Nos. P01 CA159992, R01 CA111981, and a NSF graduate fellowship. The authors want to thank Juan Santos and William Overall from HeartVista for their support through the different iterations of the authors' data acquisition platform. The authors would also like to thank Wendy Baumgardner and Yamil Saenz for their support with the authors' study and Urvi Vyas and Rachelle Bitton for their editorial help.

[a]Author to whom correspondence should be addressed. Electronic mail: jplata@stanford.edu; Telephone: +1-650-260-8531.

[1]G. Sommer, K. B. Pauly, A. Holbrook, J. Plata, B. Daniel, D. Bouley, H. Gill, P. Prakash, V. Salgaonkar, P. Jones, and C. Diederich, "Applicators for magnetic resonance–guided ultrasonic ablation of benign prostatic hyperplasia," Invest. Radiol. **48**(6), 387–394 (2013).

[2]A. J. Costello, W. G. Bowsher, D. M. Bolton, K. G. Braslis, and J. Burt, "Laser ablation of the prostate in patients with benign prostatic hypertrophy," Br. J. Urol. **69**(6), 603–608 (1992).

[3]J. C. Chen, J. A. Moriarty, J. A. Derbyshire, R. D. Peters, J. Trachtenberg, S. D. Bell, J. Doyle, R. Arrelano, G. A. Wright, R. M. Henkelman, R. S. Hinks, S.-Y. Lok, A. Toi, and W. Kucharczyk, "Prostate cancer: MR imaging and thermometry during microwave thermal ablation-initial experience," Radiology **214**(1), 290–297 (2000).

[4]H. E. Cline, J. F. Schenck, R. D. Watkins, K. Hynynen, and F. A. Jolesz, "Magnetic resonance-guided thermal surgery," Magn. Reson. Med. **30**, 98–106 (1993).

[5]K. B. Pauly, V. Rieke, L. Pisani, G. Sommer, D. Bouley, C. Diederich, A. Ross, W. Nau, A. Kinsey, C. Dumoulin, and R. Watkins, "Assessment of MR thermometry during high intensity ultrasound ablation of the canine prostate," AIP Conf. Proc. **829**, 76–80 (2006).

[6]V. Rieke and K. Butts Pauly, "MR thermometry," J. Magn. Reson. Imaging **27**(2), 376–390 (2008).
[7]W. C. Dewey, "Arrhenius relationships from the molecule and cell to the clinic," Int. J. Hyperthermia **10**, 457–483 (1994).
[8]S.-H. Shen, F. Fennessy, N. McDannold, F. Jolesz, and C. Tempany, "Image-guided thermal therapy of uterine fibroids," Semin. Ultrasound CT MRI **30**(2), 91–104 (2009).
[9]J. de. Bever, N. Todd, A. Payne, D. A. Christensen, and R. B. Roemer, "Adaptive model-predictive controller for magnetic resonance guided focused ultrasound therapy," Int. J. Hyperthermia **30**(7), 456–470 (2014).
[10]C. J. Diederich, W. H. Nau, A. Kinsey, T. Ross, J. Wootton, T. Juang, K. Butts-Pauly, V. Rieke, J. Chen, D. M. Bouley, and G. Sommer, "Catheter-based ultrasound devices and MR thermal monitoring for conformal prostate thermal therapy," in *30th Annual International Conference of the IEEE Engineering in Medicine and Biology Society, EMBS* (IEEE, 2008), pp. 3664–3668.
[11]W. C. Dewey, L. E. Hopwood, S. A. Sapareto, and L. E. Gerweck, "Cellular responses to combinations of hyperthermia and radiation," Radiology **123**(2), 463–474 (1977).
[12]P. W. Schaefer, Y. Ozsunar, J. He, L. M. Hamberg, G. J. Hunter, A. G. Sorensen, W. J. Koroshetz, and R. G. Gonzalez, "Assessing tissue viability with MR diffusion and perfusion imaging," Am. J. Neuroradiol. **24**(3), 436–443 (2003).
[13]J. Chen, B. L. Daniel, C. J. Diederich, D. M. Bouley, M. A. van den Bosch, A. M. Kinsey, G. Sommer, and K. B. Pauly, "Monitoring prostate thermal therapy with diffusion-weighted MRI," Magn. Reson. Med. **59**, 1365–1372 (2008).
[14]M. E. Ikink, M. J. Voogt, M. A. A. J. van den Bosch, R. J. Nijenhuis, B. Keserci, Y. Kim, K. L. Vincken, and L. W. Bartels, "Diffusion-weighted magnetic resonance imaging using different b-value combinations for the evaluation of treatment results after volumetric MR-guided high-intensity focused ultrasound ablation of uterine fibroids," Eur. Radiol. **24**(9), 2118–2127 (2014).
[15]M. A. Jacobs, E. H. Herskovits, and H. S. Kim, "Uterine fibroids: Diffusion-weighted MR imaging for monitoring therapy with focused ultrasound surgery—Preliminary study," Radiology **236**(1), 196–203 (2005).
[16]S. K. Das, J. Macfall, R. McCauley, O. Craciunescu, M. W. Dewhirst, and T. V. Samulski, "Improved magnetic resonance thermal imaging by combining proton resonance frequency shift (PRFS) and apparent diffusion coefficient (ADC) data," Int. J. Hyperthermia **21**(7), 657–667 (2005).
[17]A. B. Holbrook, P. Prakash, P. Jones, C. Planey, J. M. Santos, C. J. Diederich, K. Butts Pauly, and G. Sommer, "Multislice treatment planning and control for real time MR-guided prostate ablation with transurethral multisectored ultrasound applicators," in *Proceedings of International Society for Magnetic Resonance in Medicine* (2010).
[18]J. M. Santos, G. A. Wright, and J. M. Pauly, "Flexible real-time magnetic resonance imaging framework," in *26th Annual International Conference of the IEEE Engineering in Medicine and Biology Society, IEMBS* (IEEE, 2004), pp. 1048–1051.
[19]R. Bammer, "Basic principles of diffusion-weighted imaging," Eur. J. Radiol. **45**, 169–184 (2003).
[20]R. M. Goldstein, H. A. Zebker, and C. L. Werner, "Satellite radar interferometry—Two-dimensional phase unwrapping," Radio Sci. **23**, 713–720 (1988).
[21]P. Jezzard and R. S. Balaban, "Correction for geometric distortion in echo planar images from B0 field variations," Magn. Reson. Med. **34**(1), 65–73 (1995).
[22]D. Lebihan, J. Delannoy, and R. L. Levin, "Temperature mapping with MR imaging of molecular-diffusion—Application to hyperthermia," Radiology **171**, 853–857 (1989).
[23]T. V. Samulski, J. Macfall, Y. Zhang, W. Grant, and C. Charles, "Non-invasive thermometry using magnetic-resonance diffusion imaging—Potential for application in hyperthermic oncology," Int. J. Hyperthermia **8**, 819–829 (1992).
[24]S. L. Thomsen and J. E. Coad, "Developing clinically successful biomedical devices by understanding the pathophysiology of the target tissue: Insights from over 25 years at the microscope," Proc. SPIE **6440**, 644002-1–644002-15 (2007).
[25]L. X. Xu, L. Zhu, and K. R. Holmes, "Blood perfusion measurements in the canine prostate during transurethral hyperthermia," Ann. N. Y. Acad. Sci. **858**(1), 21–29 (1998).